

RESEARCH ARTICLE | JUNE 05 2025

Au@Pd nanorods with a suitable shell thickness of titanium dioxide can improve its catalytic performances ^{EP}

Yu-Chun Cheng ; Tian-Song Deng  

AIP Advances 15, 065008 (2025)

<https://doi.org/10.1063/5.0270975>View
OnlineExport
Citation

Articles You May Be Interested In

Design of homemade photoreactor for dye removal upon irradiation by sunlight

AIP Conf. Proc. (February 2021)

Microfluidic photoreactor to treat neonatal jaundice

Biomechanics (November 2021)

Sonophotocatalytic degradation of Reactive Red 120 (RR120) in the presence of TiO₂: Kinetic study

AIP Conf. Proc. (October 2016)



Special Topics Open for Submissions

[Learn More](#)

Au@Pd nanorods with a suitable shell thickness of titanium dioxide can improve its catalytic performances

Cite as: AIP Advances 15, 065008 (2025); doi: 10.1063/5.0270975

Submitted: 14 March 2025 • Accepted: 20 May 2025 •

Published Online: 5 June 2025



View Online



Export Citation



CrossMark

Yu-Chun Cheng  and Tian-Song Deng^{a)} 

AFFILIATIONS

School of Electronics and Information Engineering, Hangzhou Dianzi University, Hangzhou 310018, People's Republic of China

^{a)} Author to whom correspondence should be addressed: dengts@pku.edu.cn

ABSTRACT

The localized surface plasmon resonances (LSPRs) in plasmonic nanoparticles have been used in accelerating photocatalytic reactions under light illumination. To improve the catalytic performances, bimetallic nanoparticles composed of a plasmonic core and a catalytic shell, where LSPR-excited hot electrons and the intrinsic catalytically active sites work synergistically, have attracted much attention. Bimetallic nanostructures are a promising material for the fabrication of a novel type of photo-enhanced nanoreactor. This work presents a photoreactor based on gold–palladium (Au@Pd) nanorods with an optimized photothermal conversion and localized surface plasmon effect. Au@Pd nanorods were fabricated via a seed-mediated growth method using the surfactant hexadecylpyridiniumbromide monohydrate, making the Au@Pd surface rough, which can provide more active sites than smooth surfaces. The photothermal conversion of Au@Pd nanorods was improved with a titanium dioxide shell. Through the titanium dioxide shell, under the same light irradiation, its efficiency in catalyzing methylene blue is at most five times that of gold nanorods and at most two times that of Au@Pd nanorods.

© 2025 Author(s). All article content, except where otherwise noted, is licensed under a Creative Commons Attribution-NonCommercial 4.0 International (CC BY-NC) license (<https://creativecommons.org/licenses/by-nc/4.0/>). <https://doi.org/10.1063/5.0270975>

INTRODUCTION

Gold nanorods (Au NRs) demonstrate superior plasmonic properties in comparison to spherical particles, particularly in terms of localized electromagnetic field enhancement.¹ Au NRs exhibit transverse localized surface plasmon resonance (LSPR) perpendicular to the rod's axis, while their elongated shape enables the formation of a longitudinal LSPR along the rod's length at lower energy levels.^{2–6} This longitudinal LSPR can be readily adjusted by modifying the rods' aspect ratio (AR), allowing it to span wavelengths from visible light to the near-infrared region of the electromagnetic spectrum. This adaptability makes Au NRs highly valuable as plasmonic nanoparticles, especially for biological applications,^{7–10} as extinction by cells and tissues is minimized within this spectral range.

Compared to monometallic Au NRs, bimetallic nanorods exhibit enhanced physical and chemical properties.^{11,12} For catalytic applications, incorporating palladium (Pd) or platinum (Pt) is advantageous as these metals possess superior catalytic activity.^{13–16} Coating the nanorods with a thin layer of Pd (or Pt) can significantly

boost catalytic performance while preserving most of the plasmonic characteristics.^{17,18} The key principle involves transferring high-energy electrons generated from the plasmonic excitation of gold to the catalytic Pd layer, thereby improving its reactivity. This charge separation and plasmon-catalyst synergy in Au@Pd can be applied to various photochemical^{19,20} and electrochemical processes,^{21,22} particularly in catalytic reactions, such as reduction,²³ oxidation,²¹ coupling,²³ carbon dioxide conversion,²⁴ and nitrogen reduction.²⁵ However, the quantum efficiency of direct charge transfer in these processes remains relatively low, and the catalytic stability diminishes after extended storage periods.

Titanium dioxide (TiO₂) has long been utilized across multiple fields, including environmental protection, materials science, energy conversion, and consumer products—due to its outstanding photocatalytic activity,^{26,27} chemical stability,^{28,29} non-toxic nature,^{30,31} and versatile applications.^{32,33} As research progresses, the functionalization and potential applications of TiO₂ continue to grow, making it increasingly feasible to combine Au@Pd with TiO₂. Due to the low charge transfer efficiency of Au@Pd during reactions and

its instability after prolonged storage, as well as the fact that a continuous TiO₂ layer may suppress the catalytic activity of the particles in the absence of charge transfer to the semiconductor, TiO₂ is commonly used as a protective layer in catalytic experiments, while it also exhibits significant photothermal effects. Highly absorptive Au NRs can serve as effective photothermal agents. Due to their strong plasmonic resonance, Au NRs exhibit high absorbance, and by adjusting the aspect ratio, the absorption range can be finely tuned from the visible spectrum to the near-infrared spectrum. In addition, Pd is an excellent catalyst frequently used in many catalytic reactions. Therefore, we propose a strategy to combine Au NRs, Pd, and TiO₂ to form an Au@Pd@TiO₂ nanostructure, aimed at optimizing photothermal conversion and catalytic efficiency.

In our experiment, a coating was applied by the mild hydrolysis of titanium diisopropoxide bisacetylacetonate (TDAA) in an alkaline medium. By controlling the amount of TDAA added, we were able to form Au@Pd@TiO₂ nanoparticles with TiO₂ shells of varying thicknesses. Under the same photocatalytic experimental conditions, Au@Pd@TiO₂ exhibits significantly enhanced photocatalytic performance compared to Au NRs and Au@Pd. Specifically, the reduction rate of methylene blue (MB) by Au@Pd@TiO₂ in the presence of sodium borohydride (NaBH₄) is five times that of Au NRs and twice that of Au@Pd. Moreover, the catalytic rate of Au@Pd@TiO₂ under light irradiation is three times higher than that under dark conditions. Considering that Au@Pd shows a higher catalytic rate than Au@Pd@TiO₂ under dark conditions, we propose a synergistic mechanism: the LSPR effect of Au@Pd@TiO₂, combined with the photothermal effect of the TiO₂ shell, jointly contributes to the enhancement of its catalytic performance.

EXPERIMENTAL SECTION

Materials

Hexadecyltrimethylammonium bromide (CTAB, >98.0%) was purchased from TCI America. Sodium oleate (NaOL, >97.0%) was purchased from Shanghai Aladdin Biochemical Technology Co., Ltd. Hydrogen tetrachloroaurate trihydrate (HAuCl₄·3H₂O), L-ascorbic Acid (BioUltra, ≥99.5%), silver nitrate (AgNO₃, >99%), sodium borohydride (NaBH₄, 99%), hydrochloric acid (HCl, 37 wt. % in water), hexadecylpyridinium bromide (CPB), disodium palladium tetrachloride (Na₂PdCl₄), sodium hydroxide (NaOH, >97%), absolute methanol (MeOH), TDAA (75% in isopropanol), methylene blue (MB), and absolute ethanol were purchased from Shanghai Macklin Biochemical Technology Co., Ltd.. Ultrapure water obtained from a Milli-Q Integral system was used in all experiments. All the chemicals were used without further purification.

Synthesis of gold nanorods (Au NRs)

The seed solution for Au NR growth was prepared as follows: 0.25 ml of 10 mM HAuCl₄ was mixed with 10 ml of 0.1M CTAB solution in a 20 ml scintillation vial. 0.6 ml of fresh 0.01M NaBH₄ was diluted to 1 ml with water and was then injected into the Au (III)-CTAB solution under vigorous stirring (1200 rpm). The solution color changed from yellow to brownish yellow, and the stirring was stopped after 2 min. The seed solution was aged at room temperature for 30 min before use. To prepare the growth solution, 7.0 g (0.037M in the final growth solution) of CTAB and 1.234 g NaOL

were dissolved in 250 ml of warm water (~50 °C) in a 1 l Erlenmeyer flask. The solution was allowed to cool down to 30 °C, and 4 mM AgNO₃ solution was added. The mixture was kept undisturbed at 30 °C for 15 min after which 250 ml of 1 mM HAuCl₄ solution was added. The solution became colorless after 90 min of stirring (700 rpm), and 1.5 ml HCl (37 wt. % in water, 12.1M) was then introduced to adjust the pH. After another 15 min of slow stirring at 400 rpm, 1.25 ml of 0.064M ascorbic acid (AA) was added and the solution was vigorously stirred for 30 s. Finally, a small amount of seed solution was injected into the growth solution. The resultant mixture was stirred for 30 s and left undisturbed at 30 °C for 12 h for NR growth. The final products were isolated by centrifugation at 8000 rpm for 15 min followed by removal of the supernatant. No size and/or shape-selective fractionation was performed.

Synthesis of Au@Pd

First, Au NRs were synthesized according to the literature with slight modification and used as seed solutions. Second, 200 μl of 10 mM Na₂PdCl₄ and 2 ml Au NRs (concentrate eight times) with an aspect ratio (AR) equal to 3.6 seed solution were successively added into 20 ml of 10 mM hexadecylpyridinium bromide (CPB) solution at 65 °C. Then, 400 μl of 100 mM freshly prepared ascorbic acid (AA) solution was injected. After 2 min of vigorously stirring, the obtained solution was incubated for 30 min. Final products were collected by centrifugation at 7000 rpm for 10 min and re-dispersed in water for further use.

Synthesis of TiO₂-coated Au@Pd (Au@Pd@TiO₂)

TDAA was used as the TiO₂ precursor. Typically, by concentrating the Au@Pd solution eight times, we re-dispersed 1.2 ml of the above Au@Pd solution into 2.8 ml of DI water. 600 ml (1.5 mM) CTAB was then added to the Au@Pd solution. We controlled the solution pH to be 11 with the supplement of NaOH solution (0.1M). To the reaction solution, 20/60/80 μl of TDAA methanol solution with volume ratios of V_{TDAA}/V_{MeOH} = 3:100 (TDAA_{3,0}) was added slowly (120 μl/h) under continuous stirring at room temperature. After stirring for 3 h, the product was finally collected by centrifugation at 6000 rpm for 10 min, washed twice with water, and re-dispersed in 10 ml of MQ water.

Catalysis

Briefly, 1.0 ml of 0.01 mM MB was mixed with 0.1 ml of 50 mM freshly prepared NaBH₄, and then, 10 μl of different kinds of Au@Pd@TiO₂ solutions or 10 μl of Au NR solution was added to the mixed solution. We measured the extinction spectra of the solution at 1 min intervals until the peak corresponding to the 628 nm disappearance of the color of the solution changed from blue to transparent.

Photocatalysis

Briefly, 1 ml of 0.01 mM MB was mixed with 0.1 ml of 0.5M freshly prepared NaBH₄, and then, 10 μl of different kinds of Au@Pd@TiO₂ solutions or 10 μl of Au NR solution was added to the mixed solution. We used the above catalytic experimental steps on the basis of the illumination with a 250 W Xenon lamp (HDL-II, Suzhou Betical Optoelectronics Technology Co. Ltd., China). We measured the extinction spectra of the solution at 1 min intervals

until the peak corresponding to 628 nm disappeared. The MB concentration was determined at the wavelength of 628 nm using a UV-vis spectrophotometer (UV-1900i, Shimadzu). The reaction was maintained at normal atmospheric temperatures.

Characterization

Optical extinction spectra were recorded with a UV-1900i spectrophotometer (Shimadzu, Japan) with a 10-mm optical path. The transmission electron microscopy (TEM) images were obtained with an HT-7700 microscope (Hitachi, Japan) operating at a voltage of 100 kV. High-resolution TEM (HRTEM) images and energy-dispersive spectroscopy (EDS) mapping were performed using a Talos F200S TEM with a 200 kV acceleration voltage. The particle sizes of the nanoparticles were measured from TEM images using ImageJ software, whereby >100 nanoparticles were measured for each sample.

FDTD simulations

Finite Difference Time Domain (FDTD) is a method for solving Maxwell's equations on a discretized spatial grid in complex geometries. The FDTD simulations were carried out with commercial software (Lumerical FDTD Solutions). A total field scattered field source was used to simulate a propagating plane wave interacting with the nanostructures, with a wavelength range of 300–1400 nm. A three-dimensional nonuniform mesh was used, and a grid size of 0.5 nm was chosen for calculating the spectra and the electric field distribution of Au NR, Au@Pd, and different kinds of Au@Pd@TiO₂. In order to observe a more credible spectrum of Au@Pd@TiO₂, we choose Au NRs with a similar aspect ratio in the simulations. The dielectric functions of Au NRs were obtained by fitting the points from the data of Rioux *et al.*,³⁴ and the dielectric functions of Pd were obtained from the data of Werner *et al.*³⁵

RESULT AND DISCUSSION

Material synthesis and characterization

Figure 1(a) provides a schematic illustration of the synthesis process for Au@Pd@TiO₂ nanostructures. Initially, Au nanorods (NRs), as depicted in Fig. 1(b), are synthesized using a seed-mediated growth method. This method employs sodium oleate and

cetyltrimethylammonium bromide (CTAB) as binary surfactants, following procedures previously described in Ref. 36. The morphology and size of the synthesized Au NRs are analyzed via transmission electron microscopy (TEM), with a statistical measurement based on 100 NRs [see Figs. S1(a) and S1(b)]. The resulting Au NRs exhibit a length of 95 ± 5.0 nm and a width of 24 ± 3.0 nm, which are then used for subsequent Pd deposition.

The surfactant's structure and density significantly influence the growth of metal components, such as Ag, Pd, and Pt. For instance, CTAB shows preferential binding to the (111) plane of Au NRs, which facilitates selective growth on that surface. Additionally, a dense CTAB bilayer or a combination of sodium oleate and CTAB surfactants can inhibit further elongation of the Au NRs, while making the ends more accessible for growth.

Figure 1(c) presents the TEM image of Au@Pd nanostructures. In this step, CPB is employed to guide the deposition of Pd on the Au NRs. Palladium precursor (Na₂PdCl₄) is introduced into the purified Au NR aqueous solution, which is then washed twice at room temperature to induce Pd deposition. Ascorbic acid (AA) is added as a reducing agent. In this process, Pd²⁺ ions are initially attracted to the positively charged, CPB-coated Au NRs. AA reduces these palladium ions at the NR surface, forming a rough Pd shell. Repeated cycles of adding Pd salt followed by AA incrementally increase the thickness of the Pd clusters on the NR surface.

To further enhance the colloidal stability and improve photothermal conversion efficiency, a TiO₂ shell is grown on the surface of the Au@Pd nanostructures. The morphology of Au@Pd@TiO₂-25 can be observed in Fig. 1(d). Titanium dioxide is formed via the hydrolysis and spontaneous self-polymerization of TDDA in an alkaline buffer solution (pH 11), resulting in the formation of a shell.

Figure 2(a) presents a scanning transmission electron microscopy (STEM) high-angle annular dark-field (HAADF) image of the Au@Pd@TiO₂-25 nanostructure. The central Au NR is clearly discernible, surrounded by a Pd layer and an outer shell. Figure 2(b) provides a high-resolution TEM image, highlighting the lattice spacing of the different materials within the nanostructure. The Au NR shows a lattice spacing of 0.24 nm, aligning well with the (111) crystallographic plane, which typically has a spacing of 0.235 nm. The Pd layer, epitaxially grown on the Au NR, exhibits a lattice spacing of 0.22 nm, corresponding closely to the 0.224 nm spacing of the (111) plane for Pd. Meanwhile, the layer on the surface shows a lattice spacing of 0.23 nm, consistent with the (211) plane of anatase. As the

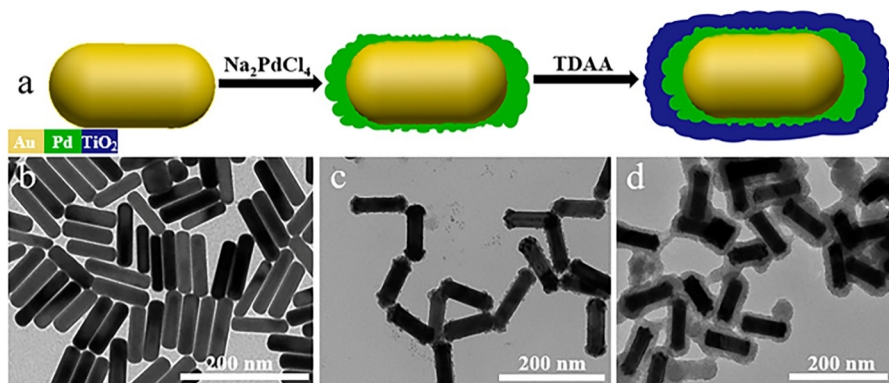


FIG. 1. (a) The schematic representation of Au@Pd@TiO₂-25: yellow is representative of Au, green signifies Pd, and blue represents TiO₂. TEM images of (b) the Au NRs, (c) the Au@Pd, and (d) the Au@Pd@TiO₂-25.

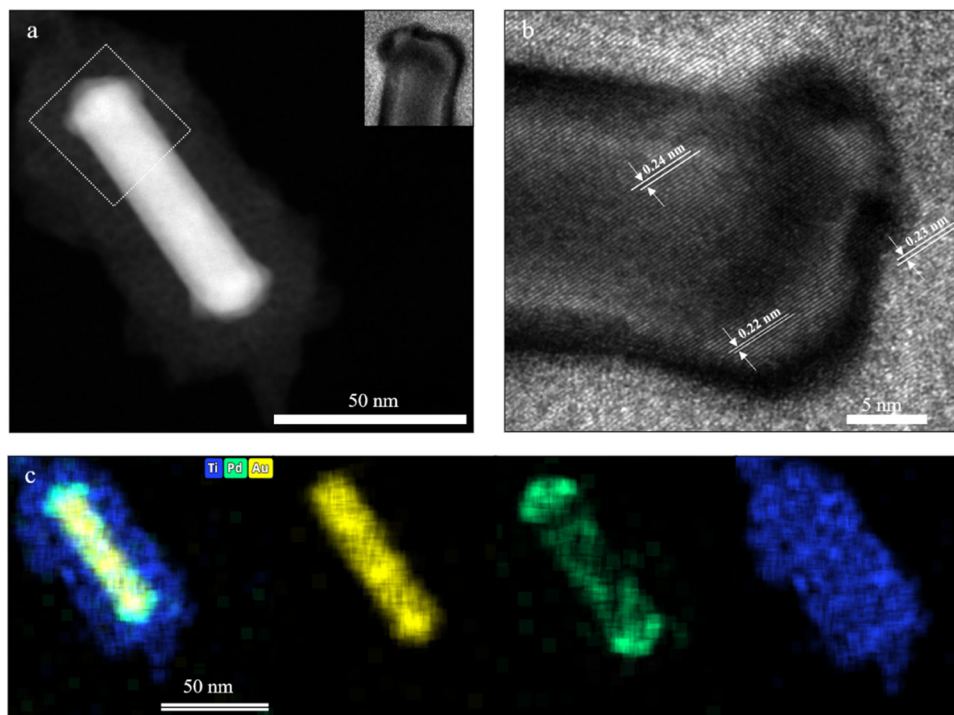


FIG. 2. (a) The STEM-HAADF image of Au@Pd@TiO₂-25. (b) HRTEM images of the Au@Pd@TiO₂-25. (c) The EDS of Au@Pd@TiO₂-25.

shell thickens, it becomes mesoporous, with rutile observed in the thicker regions. Figure 2(c) displays energy-dispersive x-ray spectroscopy (EDX) mapping, confirming the dual-core shell structure. The color-coded map distinctly shows the elemental distribution of gold (Au) and Pd, verifying the formation of the mesoporous shell. The structure's non-compact, porous morphology is clearly evident, which contributes to the enhanced catalytic performance and photothermal conversion.

Effects of shell thicknesses of TiO₂ and their plasmonic properties

As the LSPR depends strongly on the morphology, size, and composition of the nanoparticles, the modification of the Au NRs is reflected in their optical properties. The UV-vis-NIR extinction spectra of the as-prepared particles are shown in Fig. 3(a). The bare Au NRs exhibit two characteristic extinction peaks at 513 and 829 nm, corresponding to transverse and longitudinal LSPRs, respectively. The deposition of Pd particles broadens the longitudinal peak and red-shifts from 829 to 890 nm due to the additional plasmon damping caused by the palladium coating and the increased aspect ratio of the NRs. Additional coating of the Au@Pd NRs with a TiO₂ shell leads to a further red-shift and broadening as the refractive index of the shell materials is higher than that of the aqueous environment.^{37,38} A TiO₂ layer thickness of 20 ± 2.5 nm shifts the longitudinal LSPR to 985 nm, and a TiO₂ layer thickness of 25 ± 2.5 nm (30 ± 2.5 nm) shifts the longitudinal LSPR from 995 to 1010 nm. The TiO₂ layer thicknesses are shown in Figs. S2(a)–S2(c). The shifts observed in the extinction spectra confirm the successful overgrowth on the Au NRs. To maintain mild hydrolysis, 30, 60, and 90 μl of TDAA methanol solution

(V_{TDAA}/V_{MeOH} = 3:100) were gradually added to the aqueous solution of Au@Pd at a controlled rate of 120 μl/h. Consequently, the samples Au@Pd@TiO₂-20, Au@Pd@TiO₂-25, and Au@Pd@TiO₂-30 were obtained, corresponding to the respective volumes of 30, 60, and 90 μl of the TDAA methanol solution added during the hydrolysis process. TEM images reveal the successful coating of TiO₂ onto the Au@Pd surface. While some coalescence was observed, the morphology of the Au@Pd core remained unchanged, though the overall particle size increased. By varying the volume of the TDAA precursor from 30 to 90 μl, the thickness of the TiO₂ layer was precisely tuned between 20 and 30 nm, as shown in the insets of Figs. 3(b)–3(d).

Due to the photocatalytic properties of TiO₂, we initially anticipated that coating the Au@Pd nanostructures with TiO₂ would enhance their light absorption. However, the experimental results revealed the opposite: the plasmonic resonance significantly weakened after the TiO₂ coating. This unexpected behavior is likely caused by the changes in the dielectric environment of the Au@Pd nanostructures, resulting from the TiO₂ layer. The coating increased the local refractive index,^{39,40} enhancing the layer's scattering effects.^{41,42} Together, these factors not only caused a redshift of the plasmon resonance wavelength but also reduced the peak intensity.

Catalytic reduction of MB and photothermal effects of Au@Pd@TiO₂

The objective of this study is to investigate the catalytic reduction process of methylene blue (MB) and the photothermal effects of the Au@Pd@TiO₂ nanostructure. The primary aim of this research is to demonstrate a nanoscale photothermal reactor that combines

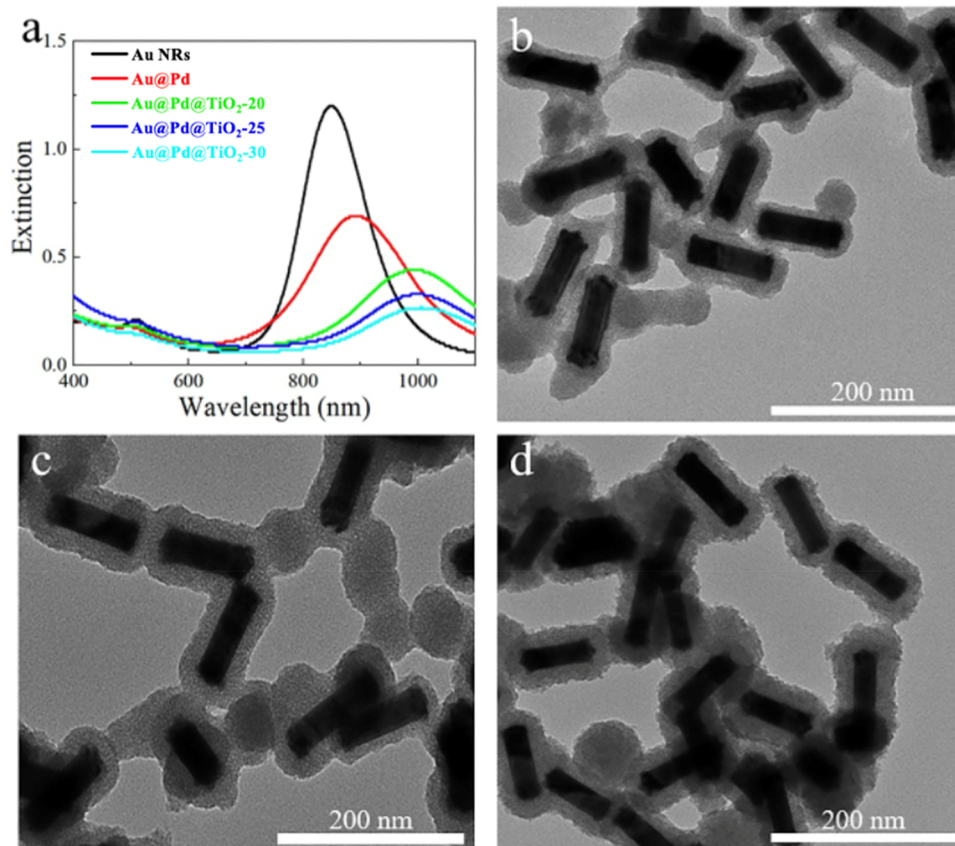


FIG. 3. (a) Spectrogram of various nanoparticles. TEM images of (b) Au@Pd@TiO₂-20 (20 nm), (c) Au@Pd@TiO₂-25 (25 nm), and (d) Au@Pd@TiO₂-30 (30 nm).

a catalyst (Pd) with an efficient photoheating source (plasmonic Au NRs) to enhance the reaction rate. Figure 4(a) provides an illustrative representation of the reaction process. In this study, we selected the reduction of methylene blue (MB) with NaBH₄ as a model reaction system under light irradiation using an Xe lamp ($\lambda > 420$ nm). Following the reduction, MB transforms into a reduced state known as leucomethylene blue, resulting in a color change from blue to colorless [as depicted in Fig. 4(b)]. To monitor the progress of the reaction, visible–near-infrared (vis–NIR) spectra were recorded over time. Since $\lambda_{\text{max}} = 628$ nm is the primary peak for changes in MB, we select the characteristic extinction peak intensity at $\lambda_{\text{max}} = 628$ nm to assess the reaction progress for more accurate results. C_0 represents the peak value corresponding to the initial MB concentration at $t = 0$ min, while C denotes the peak value at 628 nm measured at specific time intervals during the reaction process. Subsequently, we generated $-\ln(C/C_0)-t$ curves in Fig. 4(c) to visualize the reaction rates, while the thickness of the titanium dioxide shell is 25 nm.

To compare the photocatalytic performance of the Au@Pd@TiO₂ nanostructure with single metallic or bimetallic nanoparticles, we used Au NRs, Au@TiO₂, and Au@Pd to catalyze the MB reduction reaction. In a light environment, the conversion of MB was complete, with reaction times of 120 min for Au NRs and 40 min for Au@Pd. However, when Au@Pd@TiO₂-25 was

employed as a catalyst under light conditions, the response time was significantly reduced to 16 min. This observation indicated that the reaction time was greatly shortened, and the catalytic rate was substantially enhanced under light conditions. Figures S3(a)–S3(f) are the UV–vis extinction spectra of the MB reduction by NaBH₄ catalyzed with light by Au NRs, Au@TiO₂, Au@Pd, Au@Pd@TiO₂-20, Au@Pd@TiO₂-25, and Au@Pd@TiO₂-30. Figure 4(d) displays the catalytic rates of different nanoparticles, demonstrating that Au@Pd@TiO₂ exhibited the highest catalytic efficiency under light conditions. Under the same light intensity and particle density, it was at least twice as efficient as Au NRs and at least 1.2 times as efficient as Au@Pd in catalyzing the reduction of methylene blue. In certain cases, it even exceeded the catalytic efficiency of Au NRs by more than five times and was more than twice as efficient as Au@Pd. The experimental results revealed that Au@Pd@TiO₂ with a 25 nm thick titanium dioxide shell exhibited the highest efficiency. However, the rate of Au@TiO₂ is similar to that of Au NRs, mainly due to the balance between the hindering effect of the titanium dioxide shell and its photothermal effect. This balance explains why the catalytic rate of Au@Pd@TiO₂ in the MB reduction reaction does not continuously increase with the increasing thickness of the titanium dioxide shell. Nevertheless, under dark conditions, its catalytic rate was lower than that of Au@Pd but superior to Au NRs. Figures S4(a)–S4(e) display the UV–vis extinction spectra of

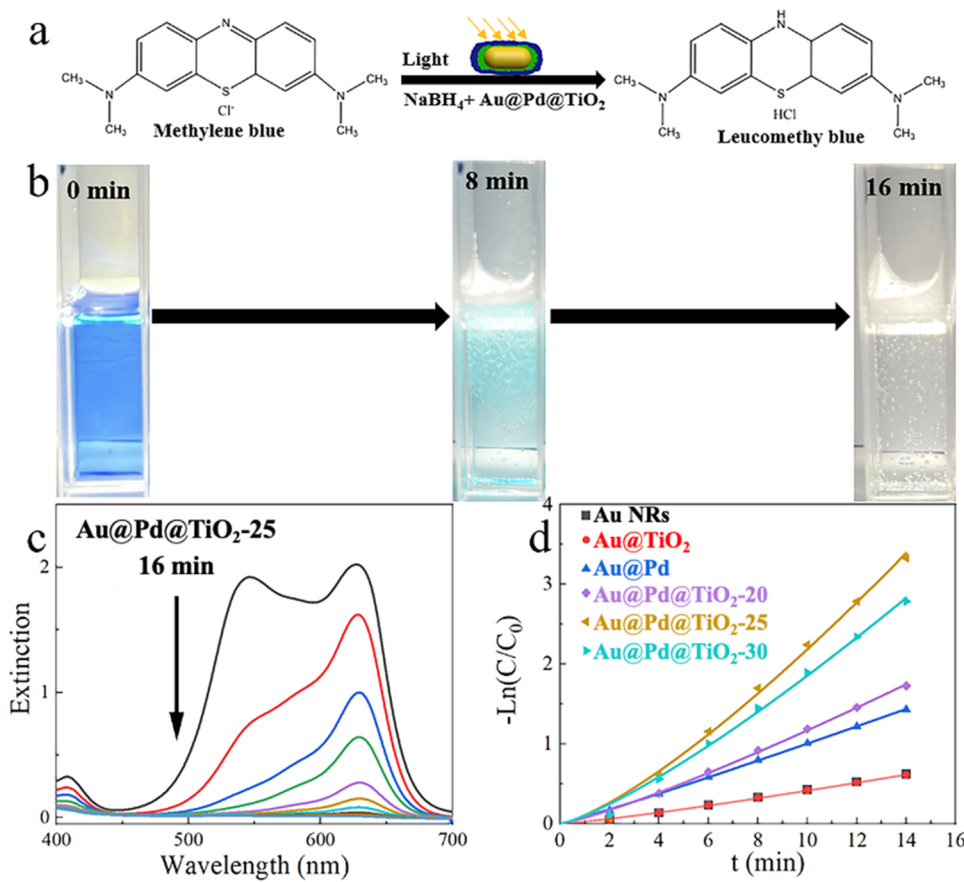


FIG. 4. (a) Scheme of MB reduced by NaBH₄ with light. The C=S and C=N bonds in the MB formula broke under the reduction of NaBH₄. (b) The MB color change process over time. (c) UV-vis extinction spectra of the MB reduction by NaBH₄ catalyzed with light by Au@Pd@TiO₂-25. (d) Photo-catalytic rate diagram of Au NRs, Au@TiO₂, Au@Pd, Au@Pd@TiO₂-20, Au@Pd@TiO₂-25, and Au@Pd@TiO₂-30.

the catalytic reduction of methylene blue (MB) by NaBH₄ without light using Au NRs, Au@Pd, Au@Pd@TiO₂-20, Au@Pd@TiO₂-25, and Au@Pd@TiO₂-30. Meanwhile, Fig. S4(f) presents a catalytic rate diagram comparing Au NRs, Au@Pd, Au@Pd@TiO₂-20, Au@Pd@TiO₂-25, and Au@Pd@TiO₂-30.

By comparing the catalytic rates of different catalysts under dark and bright conditions, it was verified that the titanium dioxide shell possessed photothermal effects. Au@Pd@TiO₂ exhibited much faster catalysis than Au@Pd under light conditions but notably slower catalysis under dark conditions. This difference could be attributed to the photothermal effect of the titanium dioxide shell in the presence of light, while in its absence, the shell hinders catalysis between the reactants at the Au@Pd active site. Additionally, the thickness of the titanium dioxide shell played a critical role in catalytic performance. Thicker shells, such as those with 30 nm thickness, led to increased diffusion barriers, resulting in a decreased catalytic rate. In contrast, thinner shells, such as 20 nm, allowed the photothermal conversion of the coated particles to surpass the diffusion barriers, while 25 nm thick shells exhibited the best photothermal conversion among them. In summary, this study highlights the significant influence of the titanium dioxide shell's thickness on catalytic performance, with thinner shells proving to be more efficient due to their superior photothermal conversion capabilities.

FDTD simulations

To find out why Au@Pd@TiO₂ showed such superior performance in photocatalysis, we performed Finite Difference Time Domain (FDTD) simulations for calculating the spectrum and electric near-field distributions at the catalytic interface for a single Au NR, Au@Pd, and Au@Pd@TiO₂-25 nanostructure. In order to compare the simulated spectrum with the experimental spectrum, we chose a gold rod similar to the experiment. Figure 5(d) shows the simulated extinction spectra, which are consistent with the experimental results, as shown in Fig. 2(d). When the Au NR is coated with a Pd shell, its frequency band will become wider and its peak will be red-shifted (from 821 to 926 nm). Due to the polydispersity and shell thickness, the peak position of titanium dioxide coated with another layer will be red-shifted (from 926 to 1060 nm), and the redshift increases with the thickening of the TiO₂ shell.

Figure 5(a) shows the electric field distribution of Au NR. As for the surface plasmon effect, the Au NR has a strong near electric field and is mainly distributed in its two ends. Figures 5(b) and 5(c) are the near electric field of Au@Pd and Au@Pd@TiO₂-25. They have the same near electric field distribution as Au NR, but it is much weaker. As control simulations, the extinction spectra as a function of TiO₂ shell thickness (20–30 nm) were simulated. The electric near-field distributions are shown in Figs. S5(a) and S5(b), and their

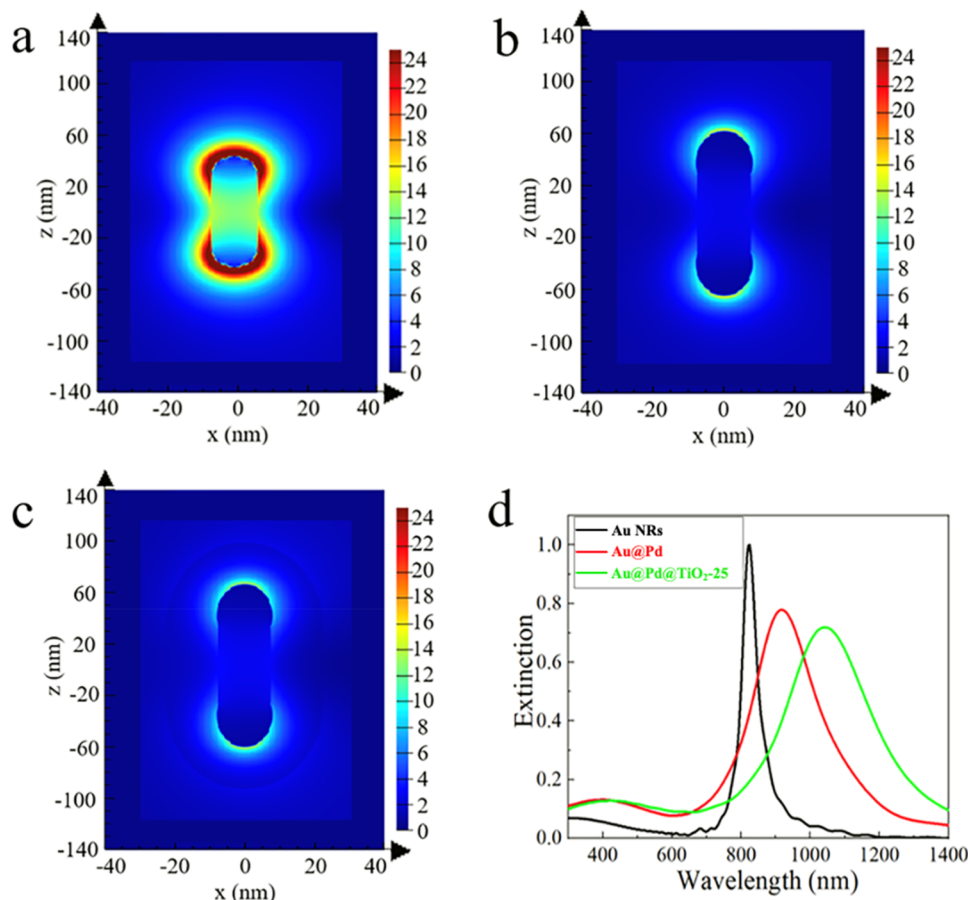


FIG. 5. FDTD simulations of electric field distributions of (a) Au NR, (b) Au@Pd, and (c) Au@Pd@TiO₂-25. (d) FDTD simulations of the spectrogram.

near-electric field changes only slightly as the TiO₂ shell thickness increases. This may be attributed to the lack of oxygen vacancies in the titanium dioxide shell layer we configured, resulting in minimal changes in the electric field.^{43,44}

In a previous study, it was also seen that the photocatalytic performance depended on the wavelength of the light. Since our work focused more on the structural differences in the reaction rates, the effects of the above-mentioned parameters on the photocatalytic reactions will be investigated in future work. Au and Pd with surface plasmon resonance properties can produce heat when exposed to light, increasing the temperature of the reaction, thus improving the energy of the reaction, and playing a catalytic role. Thus, we propose the mechanism of plasmon-mediated photocatalysis and photothermal effect as follows: First, under illumination, hot electrons can be generated in the gap between the inner Au NR and the Pd shell. Then, these high-energy hot electrons can rapidly cross the interface between Au and Pd, being transferred to the Pd. Subsequently, the hot electrons can be injected into the reaction where NaBH₄ reduces MB. Moreover, the TiO₂ shell possesses a photothermal effect, providing more energy to the inner Au NR in photocatalysis, thereby generating more hot electrons. Due to the surface plasmon effect of the Au NR, the photothermal effect of the TiO₂ shell, and the catalytic action of Pd, it exhibits excellent photocatalytic performance. In

addition, the TiO₂ shell has a photothermal effect. In photocatalysis, more energy is provided to the interior Au NR, which enables it to produce more hot electrons. Due to the surface plasmon effect of the Au NR and the photothermal effect of the TiO₂ shell, it has excellent photocatalytic performance.

CONCLUSION

In summary, we have successfully developed composite Au@Pd nanostructures stabilized with a TiO₂ coating. The particles have a surface plasmon effect and photothermal effect. Additionally, the thickness of the shell layer coated onto the Au@Pd could be precisely adjusted by changing the dosage of the precursor TDAA. Compared to Au@Pd, the shell of TiO₂ has a remarkable improvement in the photocatalysis. FDTD simulations carried out on the electric near-field distribution confirmed that the photocatalytic efficiency is improved by the co-action of the local surface plasmon effect of Au NR and the photothermal effect of the titanium dioxide shell; at the same time, the catalytic effect of Pd is also an important factor. A key parameter of photothermal enhancement catalysis is the thickness of the titanium dioxide shell. Although the thicker coating improves the photothermal effect, it also increases the barrier. Therefore, the optimal photocatalytic rate is obtained at the TiO₂ shell thickness of 25 nm. We recognize that the Au@Pd@TiO₂

material still has certain limitations, such as its relatively high cost. In the future, our research will focus on reducing the material cost by decreasing the size of noble metal particles while designing more efficient catalytic nanoparticles. Nevertheless, the excellent photocatalytic performance demonstrated by Au@Pd@TiO₂ in this study is expected to provide valuable insights for the design and development of photothermal nanoparticles, high-performance plasmonic catalysts, as well as related sensors and devices.

SUPPLEMENTARY MATERIAL

The [supplementary material](#) encompasses experimental details; size parameters of Au NRs; shell thickness of Au@Pd@TiO₂; UV–vis extinction spectra of the photocatalytic process; and electric field distributions by FDTD simulations.

ACKNOWLEDGMENTS

The authors thank Sudan Shen for her assistance in TEM at the State Key Laboratory of Chemical Engineering (Zhejiang University). The authors acknowledge financial support from the Zhejiang Provincial Natural Science Foundation (Grant No. LY24F050008), the Zhejiang Provincial Educational Ministry Scientific Research Project (Grant No. Y202352284), and the National Natural Science Foundation of China (NSFC, Grant No. 61905056).

AUTHOR DECLARATIONS

Conflict of Interest

The authors have no conflicts to disclose.

Author Contributions

Yu-Chun Cheng: Data curation (equal); Formal analysis (equal); Investigation (equal); Software (equal); Writing – original draft (equal). **Tian-Song Deng:** Funding acquisition (equal); Project administration (equal); Validation (equal); Writing – review & editing (equal).

DATA AVAILABILITY

All data generated or analyzed during this study are included in this published article and its supplementary information files.

REFERENCES

- ¹L. Shao, Y. Tao, Q. Ruan, J. Wang, and H.-Q. Lin, “Comparison of the plasmonic performances between lithographically fabricated and chemically grown gold nanorods,” *Phys. Chem. Chem. Phys.* **17**, 10861–10870 (2015).
- ²Z. He, C. Tan, Y. Li, Y. Chen, L. He, W. Liu, and Y. Liu, “Bimetallic FeCo-MOFs mediated Au nanorods etching for the multi-colorimetric and photothermal immunosensing of illegal additive,” *Talanta* **281**, 126820 (2025).
- ³S. Huang, Y. Hou, Z. Tang, M. Suhail, M. Cui, M. Z. Iqbal, and X. Kong, “Near-infrared-II responsive ovalbumin functionalized gold-genipin nanosystem cascading photo-immunotherapy of cancer,” *Nanotechnology* **35**, 365102 (2024).
- ⁴K. Li, Q. Zhang, X. Cui, Y. Liu, Y. Liu, and Y. Yang, “Photothermal-driven soft actuator capable of alternative control based on coupled-plasmonic effect,” *Chem. Eng. J.* **498**, 155057 (2024).

- ⁵J. Mahanta, S. Gupta, P. R. Parmar, D. R. Saha, C. K. Parashar, M. De, T. K. Mandal, and D. Bandyopadhyay, “Nanoplasmonic microfluidic electrolyzer for membraneless hydrogen production,” *Energy Fuels* **38**, 15701–15713 (2024).
- ⁶T. Meng, B. Li, L. Zeng, X. Sun, Y. Tian, H. Zhou, M. Zhou, and D. Li, “Plasmon coupling-driven enhanced high-order multiphoton excited fluorescent performance of metal-organic frameworks,” *Nano Res.* **17**, 6502–6508 (2024).
- ⁷A. Oladipo, T. C. Lebepe, S. Parani, R. Maluleke, V. Ncapayi, G. I. M. Mbaz, S. P. Songca, T. Kodama, and O. S. Oluwafemi, “Synthesis of NIR-II absorbing gelatin stabilized gold nanorods and its photothermal therapy application against fibroblast histiocytoma cells,” *Pharmaceuticals* **14**, 1137 (2021).
- ⁸A. O. Oladipo, *Synthesis and Photothermal Application of High Aspect Ratio Gold Nanorods* (University of Johannesburg, South Africa, 2017).
- ⁹L. Song, L. Zhang, Y. Huang, L. Chen, G. Zhang, Z. Shen, J. Zhang, Z. Xiao, and T. Chen, “Amplifying the signal of localized surface plasmon resonance sensing for the sensitive detection of *Escherichia coli* O157:H7,” *Sci. Rep.* **7**, 3288 (2017).
- ¹⁰C. Wu and Q. H. Xu, “Stable and functionable mesoporous silica-coated gold nanorods as sensitive localized surface plasmon resonance (LSPR) nanosensors,” *Langmuir* **25**, 9441–9446 (2009).
- ¹¹S. Shi, A. Li, R. Huang, J. Yu, S. Li, W. Qi, Z. He, and R. Su, “*In situ* growth of Au–Ag bimetallic nanorings on optical fibers for enhanced plasmonic sensing,” *J. Mater. Chem. C* **8**, 7552–7560 (2020).
- ¹²Y. Wei, Z. Zhao, and P. Yang, “Pd-tipped Au nanorods for plasmon-enhanced electrocatalytic hydrogen evolution with photoelectric and photothermal effects,” *ChemElectroChem* **5**, 778–784 (2018).
- ¹³S. Dutta, C. Ray, S. Sarkar, A. Roy, R. Sahoo, and T. Pal, “Facile synthesis of bimetallic Au–Pt, Pd–Pt, and Au–Pd nanostructures: Enhanced catalytic performance of Pd–Pt analogue towards fuel cell application and electrochemical sensing,” *Electrochim. Acta* **180**, 1075–1084 (2015).
- ¹⁴R. Shirai, M. Irita, T. Kurose, N. Vasiljevic, and M. Hayase, “A miniature fuel cell with monolithically fabricated Si electrodes: Application of Au–Pd–Pt multilayer catalyst,” *J. Electrochem. Soc.* **166**, D834–D842 (2019).
- ¹⁵T. T. B. Quyen, N. P. Qui, V. L. N. An, N. T. Tho, L. H. V. Thanh, B. L. A. Tuan, and T.-T. Huynh, “A novel synthesis of triangular Pt nanosheets on Pd surface with a strong electrocatalytic activity for oxidation of methanol,” *Int. J. Electrochem. Sci.* **14**, 6986–6998 (2019).
- ¹⁶J. Wang and H. Gu, “Novel metal nanomaterials and their catalytic applications,” *Molecules* **20**, 17070–17092 (2015).
- ¹⁷J. Fan, Y. Wang, L. Li, L. Gao, and L. Fan, “Layer-by-layer assembly of graphene and Au@Pt nanostructures and its application in catalytic oxidation of methanol,” *Asian J. Chem.* **26**, 5049–5052 (2014).
- ¹⁸Z. Wang, B. Dong, X. Cui, Q. Fan, Y. Huan, H. Shan, G. Feng, and Q. Fei, “Core-shell Au@Pt nanoparticles catalyzed luminol chemiluminescence for sensitive detection of thiocyanate,” *Anal. Sci.* **36**, 1045–1051 (2020).
- ¹⁹Y.-N. Dong, S.-A. Dong, and C. Tang, “Photochemical synthesis and characterization of gold @ palladium core-shell composite nanoparticles,” *Chin. J. Chem.* **30**, 1397–1401 (2009).
- ²⁰M. Lv, X. Zhang, B. Li, X. Gong, Y. Zhang, Z. Wang, Y. Liu, P. Wang, H. Cheng, Y. Dai, Y. Fan, B. Huang, and Z. Zheng, “Plasmonic Ag interlayer induced direct energy transfer studied at single-particle level,” *ACS Energy Lett.* **8**, 4033–4042 (2023).
- ²¹Y. Chen, Z. Fan, Z. Luo, X. Liu, Z. Lai, B. Li, Y. Zong, L. Gu, and H. Zhang, “High-yield synthesis of crystal-phase-heterostructured 4H/fcc Au@Pd core-shell nanorods for electrocatalytic ethanol oxidation,” *Adv. Mater.* **29**, 1701331 (2017).
- ²²Y. Zhang, J. Li, Z. Wang, H. Ma, D. Wu, Q. Cheng, and Q. Wei, “Label-free electrochemical immunosensor based on enhanced signal amplification between Au@Pd and CoFe₂O₄/graphene nanohybrid,” *Sci. Rep.* **6**, 23391 (2016).
- ²³B. H. Nguyen and V. H. Nguyen, “Recent advances in research on plasmonic enhancement of photocatalysis,” *Adv. Nat. Sci.: Nanosci. Nanotechnol.* **6**, 043001 (2015).

- ²⁴L. Q. He, H. Yang, J. J. Huang, X. H. Lu, G. R. Li, X. Q. Liu, P. P. Fang, and Y. X. Tong, "Enhanced catalytic activity of Au core Pd shell Pt cluster trimetallic nanorods for CO₂ reduction," *RSC Adv.* **9**, 10168–10173 (2019).
- ²⁵Q. Yan, L. Cao, H. Dong, Z. Tan, Y. Hu, Q. Liu, H. Liu, P. Zhao, L. Chen, Y. Liu, Y. Li, and Y. Dong, "Label-free immunosensors based on a novel multi-amplification signal strategy of TiO₂-NGO/Au@Pd hetero-nanostructures," *Biosens. Bioelectron.* **127**, 174–180 (2019).
- ²⁶Y. Li, S. G. Li, J. Wang, Y. Li, C. H. Ma, and L. Zhang, "Preparation and solar-light photocatalytic activity of TiO₂ composites: TiO₂/kaolin, TiO₂/diatomite, and TiO₂/zeolite," *Russ. J. Phys. Chem.* **88**, 2471–2475 (2014).
- ²⁷D. R. Zhang, H. L. Liu, S. Y. Han, and W. X. Piao, "Synthesis of Sc and V-doped TiO₂ nanoparticles and photodegradation of rhodamine-B," *J. Ind. Eng. Chem.* **19**, 1838–1844 (2013).
- ²⁸H. Sohn, S. Kim, W. Shin, J. M. Lee, H. Lee, D.-J. Yun, K.-S. Moon, I. T. Han, C. Kwak, and S.-J. Hwang, "Novel flexible transparent conductive films with enhanced chemical and electromechanical sustainability: TiO₂ nanosheet-Ag nanowire hybrid," *ACS Appl. Mater. Interfaces* **10**, 2688–2700 (2018).
- ²⁹Q. H. Xia, S. Kawi, K. Hidajat, and L. L. Li, *Recent Advances in the Science and Technology of Zeolites and Related Materials, Pts a–C* (Elsevier Science B.V., Cape Town, South Africa, 2004).
- ³⁰S. Babitha and P. S. Korrapati, "Biosynthesis of titanium dioxide nanoparticles using a probiotic from coal fly ash effluent," *Mater. Res. Bull.* **48**, 4738–4742 (2013).
- ³¹K. S. Venkataprasanna, J. Prakash, T. Anusuya, and G. Devanand Venkatasubbu, "Size dependent mechanistic activity of titanium dioxide nanoparticles for enhanced fibroblast cell proliferation and anti-bacterial activity," *J. Sol-Gel Sci. Technol.* **99**, 565–575 (2021).
- ³²J. Ding, J. Zhao, H. Zhang, and S. Dong, "Bias-free glucose/O₂ bio-photoelectrochemical system for multi-energy conversion and phenolic pollutant degradation," *Biosens. Bioelectron.* **266**, 116714 (2024).
- ³³Z. Rabbani, M. U. Khan, A. Anwar, A. U. Hassan, and N. Alhokbany, "Synergistic charge-transfer dynamics of novel D-D-A- π -A framework containing indoline-benzo[d][1,2,3]thiazole based push-pull sensitizers: From structural engineering to performance metrics in photovoltaic solar cells," *J. Mol. Model.* **30**, 338 (2024).
- ³⁴D. Rioux, S. Vallieres, S. Besner, P. Munoz, E. Mazur, and M. Meunier, "An analytic model for the dielectric function of Au, Ag, and their alloys," *Adv. Opt. Mater.* **2**, 176–182 (2014).
- ³⁵W. S. M. Werner, K. Glantschnig, and C. Ambrosch-Draxl, "Optical constants and inelastic electron-scattering data for 17 elemental metals," *J. Phys. Chem. Ref. Data* **38**, 1013–1092 (2009).
- ³⁶Y. Qiu, Y. Liu, L. Wang, L. Xu, R. Bai, Y. Ji, X. Wu, Y. Zhao, Y. Li, and C. Chen, "Surface chemistry and aspect ratio mediated cellular uptake of Au nanorods," *Biomaterials* **31**, 7606–7619 (2010).
- ³⁷J. A. Jurado-González, E. G. Lizárraga-Medina, J. Vazquez, O. Romo, J. López, O. E. Contreras-López, N. Nedev, H. Márquez, and H. Tiznado, "TiO₂-x films as a prospective material for slab waveguides prepared by atomic layer deposition," *Opt. Laser Technol.* **158**, 108880 (2023).
- ³⁸Y. Wang, M. I. Tejedor-Tejedor, W. Tan, and M. A. Anderson, "Influence of solution chemistry on the dielectric properties of TiO₂ thin-film porous electrodes," *J. Phys. Chem. C* **120**, 21543–21551 (2016).
- ³⁹J. Dong, S. Chen, G. Huang, Q. Wu, X. Huang, L. Wang, Y. Zhang, X. Ao, and S. He, "Low-index-contrast dielectric lattices on metal for refractometric sensing," *Adv. Opt. Mater.* **8**, 2000877 (2020).
- ⁴⁰R.-B. Wei, C.-H. Zhan, Y. Yang, P.-L. He, and X.-B. Liu, "Polyarylene ether nitrile and titanium dioxide hybrids as thermal resistant dielectrics," *Chin. J. Polym. Sci.* **39**, 211–218 (2020).
- ⁴¹H. Liu, W. Jiang, L. Yin, Y. Shi, B. Chen, W. Jiang, and Y. Ding, "Enhanced photovoltaic performance of dye-sensitized solar cells with TiO₂ micro/nano-structures as light scattering layer," *J. Mater. Sci.: Mater. Electron.* **27**, 5452–5461 (2016).
- ⁴²Y. Liu, C.-Y. Liu, Z.-Y. Zhang, and C.-Y. Wang, "The surface enhanced Raman scattering effects of composite nanocrystals of Ag-TiO₂," *Spectrochim. Acta, Part A* **57**, 35–39 (2001).
- ⁴³S. Huang, J. Wang, R. Bao, J. Yi, L. Liu, and X. Kong, "Oxygen vacancy-induced modulation of the built-in electric field of TiO₂- α /WO₃- δ for enhanced CO₂ photoreduction," *Ceram. Int.* **50**, 38323–38330 (2024).
- ⁴⁴D. Zuo, W. Meng, C. Fan, T. Li, S. Deng, D. Li, L. Jiang, and T. Wang, "Heterogeneous interface design with oxygen vacancy-rich assistance high-capacity titanium-based oxide anode materials for sodium-ion batteries," *ACS Appl. Mater. Interfaces* **16**, 52559–52571 (2024).